**SANDIA REPORT** SAND2022-6534 Printed May 2022



Impact Response of Control Atmosphere Plasma Spray Deposited Materials

Brittany A. Branch, Chad McCoy and Andrew Vackel

Prepared by Sandia National Laboratories Albuquerque, New Mexico 87185 and Livermore, California 94550 Issued by Sandia National Laboratories, operated for the United States Department of Energy by National Technology & Engineering Solutions of Sandia, LLC.

**NOTICE:** This report was prepared as an account of work sponsored by an agency of the United States Government. Neither the United States Government, nor any agency thereof, nor any of their employees, nor any of their contractors, subcontractors, or their employees, make any warranty, express or implied, or assume any legal liability or responsibility for the accuracy, completeness, or usefulness of any information, apparatus, product, or process disclosed, or represent that its use would not infringe privately owned rights. Reference herein to any specific commercial product, process, or service by trade name, trademark, manufacturer, or otherwise, does not necessarily constitute or imply its endorsement, recommendation, or favoring by the United States Government, any agency thereof, or any of their contractors or subcontractors. The views and opinions expressed herein do not necessarily state or reflect those of the United States Government, any agency thereof, or any of their contractors.

Printed in the United States of America. This report has been reproduced directly from the best available copy.

Available to DOE and DOE contractors from

U.S. Department of Energy Office of Scientific and Technical Information P.O. Box 62 Oak Ridge, TN 37831

Telephone: (865) 576-8401 Facsimile: (865) 576-5728 E-Mail: reports@osti.gov

Online ordering: <a href="http://www.osti.gov/scitech">http://www.osti.gov/scitech</a>

Available to the public from

U.S. Department of Commerce National Technical Information Service 5301 Shawnee Rd Alexandria, VA 22312

Telephone: (800) 553-6847 Facsimile: (703) 605-6900 E-Mail: orders@ntis.gov

Online order: <a href="https://classic.ntis.gov/help/order-methods/">https://classic.ntis.gov/help/order-methods/</a>



### **ABSTRACT**

Thermal spray processing of metals and respective blends is becoming increasingly attractive due to the unique properties such as increased yield strength, low ductility, and differences in tensile and compressive strengths that result from microstructural features due to the spray process compared to other additive manufacturing methods. Here we report the results of plate impact experiments applied to Controlled Atmosphere Plasma Spray deposits of tantalum (Ta), niobium (Nb), and a tantalum-niobium blend (TaNb). These methods allowed for definition of the Hugoniot for each material type and the assessment of the Hugoniot Elastic Limit (HEL). Spallation experiments were conducted, and soft recovery of each material type allowed for scanning electron microscopy to characterize the fracture mechanism during tensile loading.

# **ACKNOWLEDGEMENTS**

We would like to thank Lena Pacheco, Josh Usher, Keith Hodge and Steven Dean at the Dynamic Integrated Compression Experimental (DICE) facility for experimental support. Also, Tom D Holmes and Celedonio Jaramillo for their material fabrication support at the Thermal Spray Research Laboratory.

# TABLE OF CONTENTS

Abstract3
Acknowledgements
List of Figures5
List of Tables6
Introduction7
Experimental Methods9
Controlled Atmosphere Plasma Spray Sample Fabrication9
Gas Gun Target Fabrication10
Ultrasonic Sound Speed Measurements
Results & Discussion14
Conclusions32
References
Distribution
LIST OF FIGURES
Figure 1 Cut-away view of SG-100 Plasma torch (from Praxair Surface Solutions)
Figure 5. Velocity histories measured at the impactor/window interface for Ta deposited by controlled atmosphere plasma spray and impacted in a reverse-ballistic configuration at low (left) and high (right) impact velocities
Figure 6. Velocity histories measured at the impactor/window interface for Nb deposited by controlled atmosphere plasma spray and impacted in a reverse-ballistic configuration at low (left) and high (right) impact velocities
Figure 7. Velocity histories measured at the impactor/window interface for Ta/Nb blend deposited by controlled atmosphere plasma spray and impacted in a reverse-ballistic configuration at low (left) and high (right) impact velocities
Figure 8. Hugoniot stress as a function of shock-induced particle velocity for controlled atmosphere plasma spray-deposited materials with the linear Rankine-Hugoniot fit for Ta (A), Nb (B) and TaNb (C), respectively
Figure 9. Hugoniot stress as a function of shock-induced particle velocity for air, cold, and controlled atmosphere spray-deposited materials for Ta, Nb and TaNb, respectively. For the pure Ta and Nb materials the solid Hugoniot is also shown

Figure 10: Wave profiles measured at sample-window interface for transmitted wave shots. HEL velocities were similar for both the higher velocity DG652 shot (left, panels A-C) and the	
lower velocity DG653 shot (right, panels D-F). Steady peak states were not observed for Ta	_
on DG652 or Ta and TaNb on DG653	U
Figure 11: Impedance matching diagram for CAPS tantalum samples on transmitted wave shots.	
The sapphire window is higher impedance than the sample and a reshock is reflected back into the material	2
Figure 12. Free-surface velocity histories measured for cold spray-deposited samples subjected to	
a sapphire impact at the specified velocities. Circle indicates the transition from elastic to plastic deformation	3
Figure 13: 100x magnification of tantalum fracture surface showing a single large spall plane	
through the center of the image.	6
Figure 14: The 1000x magnification of tantalum fracture surface shows signs of plastic	
deformation between locations where fracture followed splat boundaries	7
Figure 15: Low-magnification image of spall plane in Niobium sample. A clear spall plane is	
present, however the damage sites have not coalesced and induced complete spall2	8
Figure 16: 1300x magnification image of nucleated void in niobium	9
Figure 17: 30× magnification image of spall plane in TaNb blend sample3	0
Figure 18: 1000× image of crack in damage site of Ta-Nb blend sample	1
LIST OF TABLES	
Table 1 SG-100 plasma torch settings used for sample synthesis	9
Table 2. Density ( $\underline{\rho 0}$ ), longitudinal acoustic wave speed ( $\underline{cL}$ ) and shear acoustic wave speed ( $\underline{cs}$ ) for CAPS materials used in this study.	
Table 3. Calculated Elastic Constants derived from measured longitudinal and shear wave speeds1.	
Table 4. Summary of measured projectile $(u_0)$ , average interface velocity measured $(u_{Avg})$ , the	
particle velocity $(u_p)$ , and the calculated Hugoniot stress $(\sigma_{Hug})$ and strain $(\varepsilon_{Hug})$ for Ta, Nb,	
and TaNb with initial density given ( <u>oo</u> ).	5
Table 5: Sample, impactor, and window metrology for transmitted wave shots1	
Table 6: Impact velocity, elastic wavespeed, peak stress, and Hugoniot elastic limit for samples on transmitted wave shots	
Table 7. Hugoniot elastic limit stress, pressure, yield strength and shear stress are shown for	
CAPS materials2	3
Table 8. Peak free surface velocity ( $\underline{ufs}$ ), pullback velocity ( $\underline{\Delta ufs}$ ), and calculated spall strength ( $\underline{\sigma sp}$ ) for CAPS samples.	4
	-

#### **INTRODUCTION**

Advanced manufacturing provides a means to realize materials with unique geometries and tailored material properties. Thermal spraying of metals is becoming increasingly attractive compared to conventional high temperature processes such as additive manufacturing and laser/electron beam deposition due to the process minimizing oxidation<sup>1,2</sup> of the powder during deposition thus resulting in lower residual tensile stress,<sup>3</sup> cracks, and distortion.<sup>4-7</sup> Also thermal spray deposition allows for engineering to reduce or eliminate the heat effective zone in substrates, making it the preferred technique for joining dissimilar materials. Within the broader Thermal Spray (TS) processing family there are a variety of techniques including Air [Plasma] Spray (AS),<sup>8,9</sup> Cold Spray (CS)<sup>5,10</sup> and Controlled Atmosphere Plasma Spray (CAPS).<sup>6,11</sup> These deposition methods either utilize kinetic-based deposition<sup>12</sup> in the case of CS or melt deposition via a direct current plasma torch in either air or a controlled argon environment in the case of AS and CAPS, respectively.<sup>13</sup>

For the last few years there has been a concerted effort to stand up a comprehensive Thermal Spray Lab at Sandia National Laboratory (Department 1834). These efforts have included the extensive study of the material property dependence of the varying deposition methods. Overall spray deposits exhibit higher dislocation densities resulting in a higher degree of anisotropy thus increasing the yield strength, lowering the ductility, and enabling unique tensile and compressive strengths. Pace These material properties are expanding the application of TS metals towards structural components that require unique mechanical properties to mitigate shock and vibration. As an example, CS metals have shown unique mechanical properties including improved fatigue properties due to increased hardness under crack initiation and increased bending in growth tests as a result of higher plasticity and local ductility. One recently, studies have extended the mechanical load towards higher strain rates for AS and CS where the Hugoniot, Hugoniot Elastic Limit and spallation fracture mechanism as a result of tensile loading have been reported for deposits composed of tantalum (Ta), niobium (Nb), and a tantalum-niobium blend (TaNb).

Because there is limited knowledge of TS metals subjected to dynamic loading, we chose to extend our previous studies on CS materials<sup>31</sup> to CAPS deposited films similar in composition. Historically, wrought and additively-manufactured tantalum have been extensively studied under dynamic compression over a range of pressures, but there has been little effort to understand microstructural dependence of dynamic behavior.<sup>33-38</sup> Extending these studies to CAPS deposited materials in comparison to previously tested AS<sup>30</sup> and CS<sup>31,32</sup> deposits allows us to decouple the response of the material from the microstructure and enable understanding of behavior specific to materials fabricated with varying processing techniques. We included niobium due to it being a low-density principal refractory metal and having similar properties to tantalum at an initial density of about half of Ta.<sup>39</sup> Also, niobium is of interest because it has been shown to increase strength in alloys of refractory metals.<sup>40</sup> To this end, the co-sprayed blend was used to test whether niobium inclusion through CAPS deposition would enhance adhesion between layers of the two dissimilar metals or the interfaces would act as weak points in the coating.

Shock compression experiments were conducted to measure the differences in the fundamental material properties including the principle Hugoniot and the spall strength of the three materials respectively. The principle Hugoniot of CAPS deposited material for all three compositions were compared to AS and CS deposits similar in composition. Postmortem materials characterization was conducted to investigate the primary fracture mechanisms of CAPS deposited materials during tensile loading. These results provide insight into the effects that microstructure resulting from TS

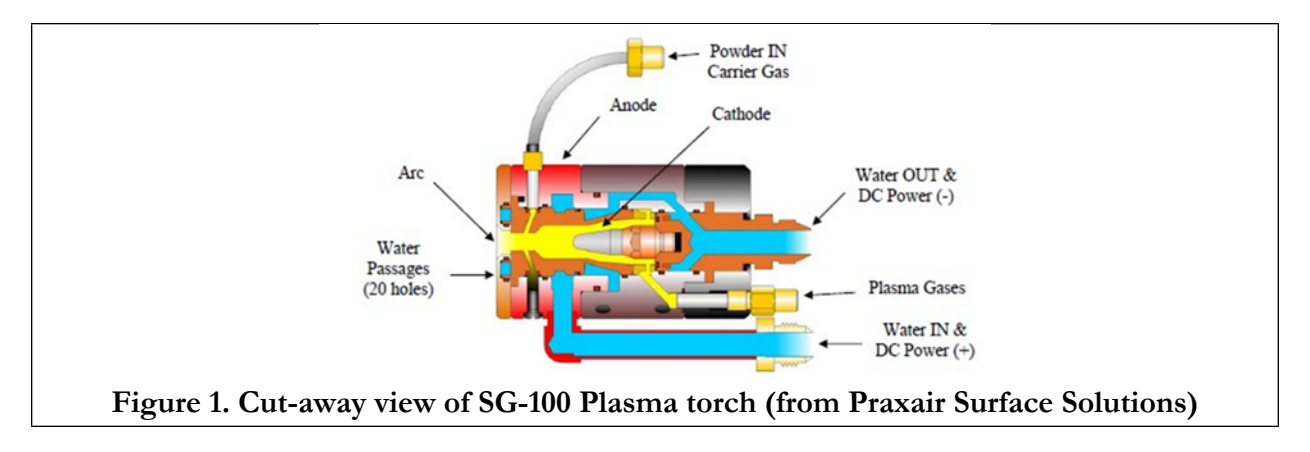
techniques has on the dynamic performance compared to traditional manufacturing and higher temperature additive techniques and provides a base for the development of structural component materials with unique mechanical properties for aerospace and military applications.

#### **EXPERIMENTAL METHODS**

## Controlled Atmosphere Plasma Spray Sample Fabrication

Samples were fabricated using the Controlled Atmosphere Plasma Spray (CAPS) method utilizing a commercially available direct current plasma spray torch to continually melt and accelerate powdered feedstock material to create a shower of molten particles that is translated over a prepared substrate surface. Particles rapidly impinge, spread, solidify, and cool to form a lamellar-like microstructure. Repeated translations of the particle stream over the substrate are used to achieve desired deposit thicknesses, which can range from tens of micrometers to milli-meters. What makes CAPS unique from other melt deposition TS process (such as plasma spray performed in an open-air environment) is that the controlled atmosphere aspect can be used to deposit materials in inert gas environments (i.e., argon) thereby minimizing oxidation of sprayed material.

The CAPS system operated by SNL Org. 1834 currently consists of a commercially available SG-100 plasma spray torch housed within a vacuum chamber that is capable of being evacuated and being backfilled with either nitrogen or argon and operated in the range of medium vacuum to slightly above atmospheric pressure. The primary gas used for SG-100 operation is ultra-high purity argon with helium for a secondary gas. Powder is delivered by a separate argon gas flow. A schematic of the SG-100 plasma spray torch is shown in Figure 1. Further details of the CAPS system operated by SNL Org. 1834 can be found in.<sup>41,42</sup>



The same torch parameter settings were used for all CAPS deposits within this study and are given in Table 1. Prior to initiating the CAPS process, the chamber was evacuated to a pressure of less than 150 mTorr followed by backfilling with ultra-high purity argon to a pressure of 640 Torr (atmospheric pressure at Albuquerque NM is 630 Torr), which was maintained during spraying by a butterfly valve with feedback control.

Table 1 SG-100 plasma torch settings used for sample synthesis

Hardware [Anode/Cathode/Gas Ring]	Amperage [A]	Primary Gas (Ar) [slpm]	Secondary Gas (He) [slpm]	Powder Injection Port	Powder gas (Ar) [slpm]
Standard (730/720/112)	540	50	12	Internal	3.0

Commercially available Amperit 150.074 and Amperit 160.074 powders¹ were used for the tantalum and niobium deposits, respectively. These same powders were used for Cold Spray sample synthesis.⁴³ Both powders are advertised as a "fused and crushed" morphology. The nominal particle size range for both powders is given as 15 to 45 µm (designated by the ".074" within the product code). For the blended deposits, the tantalum and niobium powders were physically mixed at the desired ratios by a V-blender and then fed from a single powder hopper. Powder feed rate during deposition was controlled by the rotational speed of the powder hopper's metering disk and the mass flow rate was measured independent from the deposition process by weighing the amount of powder dispensed over several minutes. The measured powder feed rates were 32.5g/min for tantalum, 15g/min for niobium, and 25.5g/min for the blended powder. Duplicate samples of tantalum, niobium, and blended tantalum-niobium using the same materials and processing parameters (referred to as the "S/N Low" parameter) were synthesized and had their microstructure and thermo-physical properties characterized as part of an independent study and are previously documented.⁴²

A rotating fixture that had been previously designed and built to collect thick deposits of CAPS material was used to mount four aluminum (Al) and four stainless steel (SS) coupons. These coupons were continuously rotated while simultaneously being translated under the torch's particle stream to collect a deposit as evenly as possible to the desired thickness (greater than 3.5mm). The coupons were approximately 75mm wide, 63mm tall, and 9mm thick. The surface area of the coupons was selected to interface with the existing fixture's dimensions and so that wire electrodischarge machining (EDM) would be able to yield a 45mm diameter disc of deposit and substrate from each coupon. Coupon thickness was chosen to minimize any warping that would occur from the residual stress of the deposit. To help meet the sample dimension requirements of parallelism and flatness, the coupons were specified to a surface parallelism of less than 15 to 20µm and a flatness of less than 10µm. Before and after coupon thickness measurements were made to ensure adequate thickness was collected. The coupons were then wire EDM cut to make 45mm and 19 mm diameter cylinders of deposit and substrate which were then subjected to grinding and polishing to yield polished discs of CAPS deposits without a substrate for further testing. The method of grinding and polishing the substrate away instead of using wire EDM to liberate the CAPS material from the substrate was adopted to minimize previously encountered non-parallelism found in cut samples, which is likely due to the relaxation of the deposit's residual strain during the wire EDM process.

## Gas Gun Target Fabrication

CAPS material was incorporated into the projectile for reverse-ballistic tests to probe Hugoniot states in the configuration shown in Figure 2. The CAPS material was cut to a nominal diameter of 45 mm and the respective thickness are shown below in Table 4. The CAPS samples were used as impactors and simultaneously struck three witness windows (PMMA, LiF, and c-cut sapphire) mounted adjacent to one another in an aluminum target-support ring. This configuration yielded Hugoniot data for three separate peak stresses resulting from a single impact velocity and the respective shock impedances of PMMA <sup>44</sup>, LiF <sup>45</sup>, and Sapphire <sup>44,46</sup>, respectively. For all shots, the incident velocity of the aluminum projectile nosepiece and its embedded CAPS impactor relative to

-

<sup>&</sup>lt;sup>1</sup> Presently sold by Höganäs. The previous owner of the Amperit brand, H.C. Starck, was the supplier of the tantalum powder used for this study while the niobium was purchased from Höganäs. There is not expected to be major differences in the powder characteristics or quality based on the Amperit brand owner.

the stationary target assembly that incorporated the three windows was determined based on the arrival-time signals from an array of electrically charged pins located around the target periphery, we note that absolute timing fiducials were not cross-timed between pins and VISAR. A velocity interferometer system, VISAR <sup>47</sup>, provided time-resolved velocity data for each impactor/window interface. Optical delay settings for the interferometer were specified in order to provide data corresponding to dual velocity per fringe (VPF) constants of 0.070 (Low: T15, T17, T19) and 0.090 (High: T16, T18, T20) in vacuum, resulting in a complementary pair of velocity histories (*i.e.*, wave profiles) for each window type. Impact times were determined from the VISAR fiducial signal and subtracted to obtain time zero for the velocity histories reported here.

In addition, forward-ballistic experiments were performed to measure the transmitted wave profile through all three sample types backed by a window and free surface. Windowed measurements were fielded with time of arrival probes to determine the impact time on the samples and calculate the shock speed from the transit time. Experiments used a triple-sample configuration with a sapphire impactor and 12-mm-thick c-cut sapphire windows on the samples as shown in Figure 3. One sample of each type was included on each experiment. Two experiments with different impact velocities (~170 and ~230 m/s) were conducted to identify any strain-rate dependence on the Hugoniot Elastic Limit. Interferometer settings were the same as used for the reverse-ballistic tests. Details of the diagnostic co-timing for transit time measurement are described previously.<sup>32</sup>

In the free surface transmitted wave experiments the sample and impactor thicknesses were optimized to induce spall (tensile stress) in the CAPS sample. We report a total of three experiments according to the configuration shown in Figure 4, where a sapphire impactor (dimensions specified in Table 5) struck a CAPS sample at an average velocity of 0.172 km/s. VISAR instrumentation monitoring the free (*i.e.*, rear) surface motion of the sample yielded a pair of velocity histories for VPF settings of 0.080 (T16) and 0.100 (T15) km/s in vacuum, respectively.

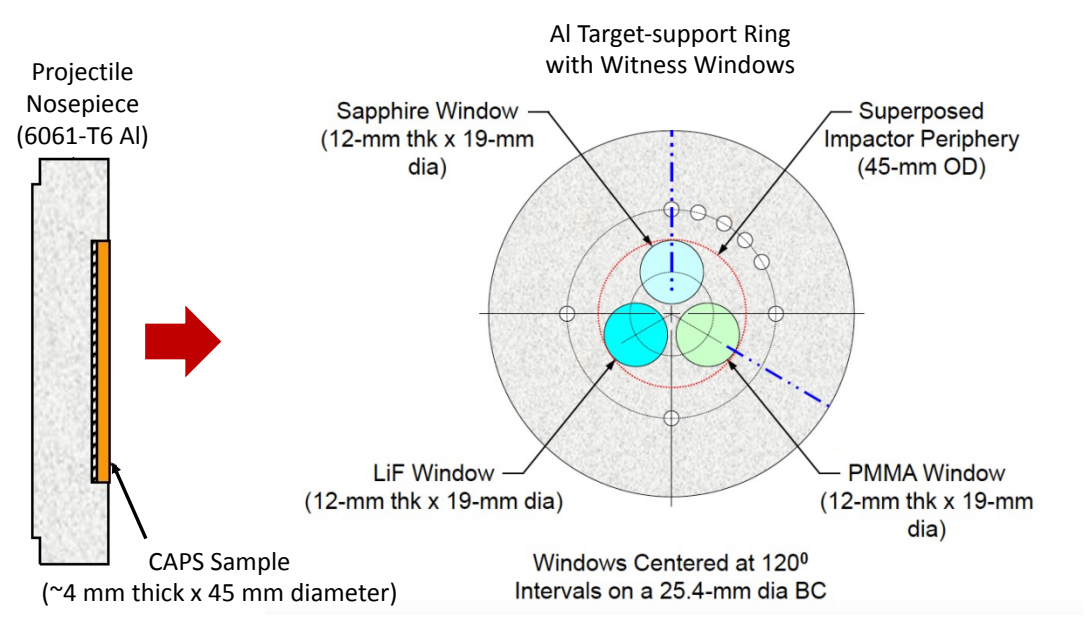


Figure 2. Reverse-ballistic configuration for Hugoniot measurement on CAPS deposits. [Image adapted from J.L. Wise]

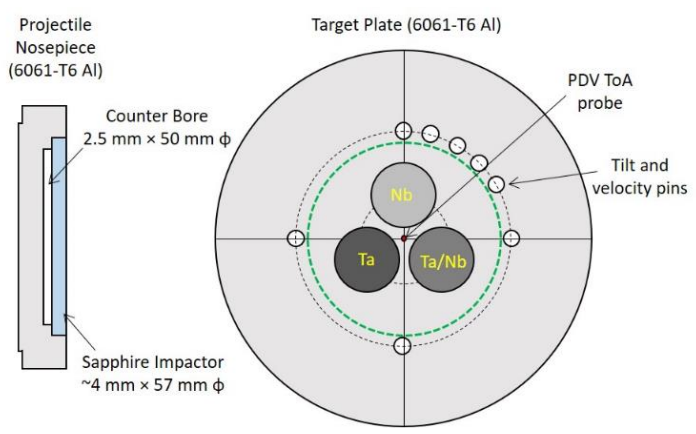


Figure 3: Forward-ballistic configuration used for transmitted wave measurements on CAPS materials. 12-mm-thick sapphire windows (not shown) were included on all samples.

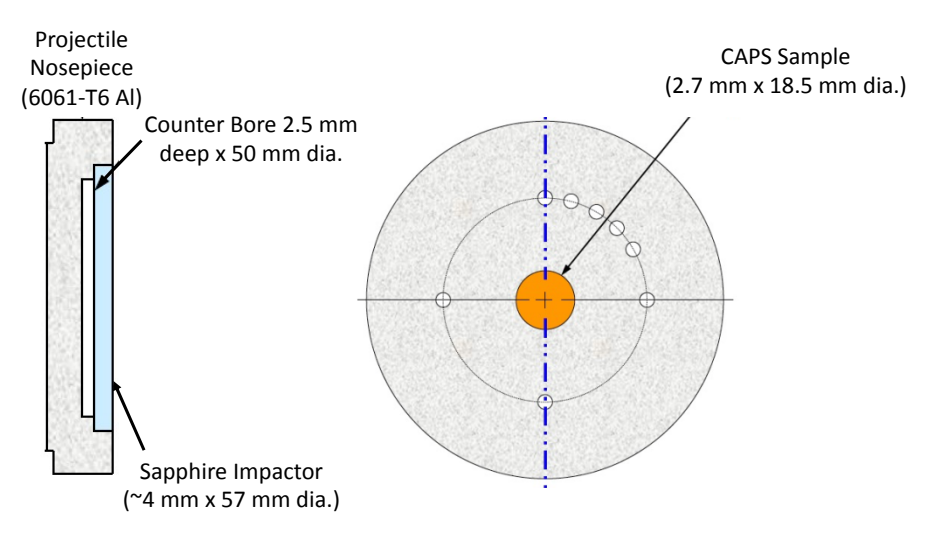


Figure 4. Forward-ballistic configuration for transmitted wave measurement on CAPS deposits backed by a sapphire window or free-surface to measure spall strength. [Image adapted from J.L. Wise]

### **Ultrasonic Sound Speed Measurements**

Density and ultrasonic sound speed measurements were conducted on CAPS samples in a previous study at the non-destructive testing laboratory or the DICE facility at SNL.<sup>48</sup> The measured density, longitudinal and shear sound speeds are shown in

Table 2. The corresponding elastic constants derived from these values are shown in Table 3.

Table 2. Density  $(\rho_0)$ , longitudinal acoustic wave speed  $(c_L)$  and shear acoustic wave speed  $(c_S)$  for CAPS materials used in this study.

Sample Type	Density $ ho_o$ (g/cc)	Longitudinal Wave Speed c <sub>L</sub> (km/s)	Shear Wave Speed c <sub>s</sub> (km/s)
Та	15.159	1.584	1.307
Nb	7.826	2.858	1.918
TaNb	11.854	2.226	1.649

Table 3. Calculated Elastic Constants derived from measured longitudinal and shear wave speeds.

Sample	Calculated	Calculated	Calculated	Calculated	Calculated
Type	Poisson's	Bulk Wave	Shear	Bulk	Young's
	Ratio	Speed	Modulus	Modulus	Modulus
	ν	$c_o(km/s)$	G (GPa)	K (GPa)	E (GPa)
Ta	-0.567	0.481	25.895	3.510	22.447
Nb	0.090	1.806	28.790	25.538	62.778
TaNb	-0.108	1.153	32.233	15.760	57.499

## **RESULTS & DISCUSSION**

Reverse-ballistic Hugoniot experiments were conducted on the three sample types. Figure 5-8 shows the measured velocity history for each sample at an impact velocity ranging from 0.17 - 0.3 km/s. Independent of material type the velocity can be characterized by a steep rise followed by initial plateau. The non-equilibrium material response at later times may be due to heterogeneity of the CAPS material, the arrival of a longitudinal release wave resulting from the interface of the sample and the nosepiece of the projectile, or the arrival of a lateral edge release wave from the periphery of the window. As stated previously, for each window type there were two free-surface VPF constants (above) indicated by the legend.

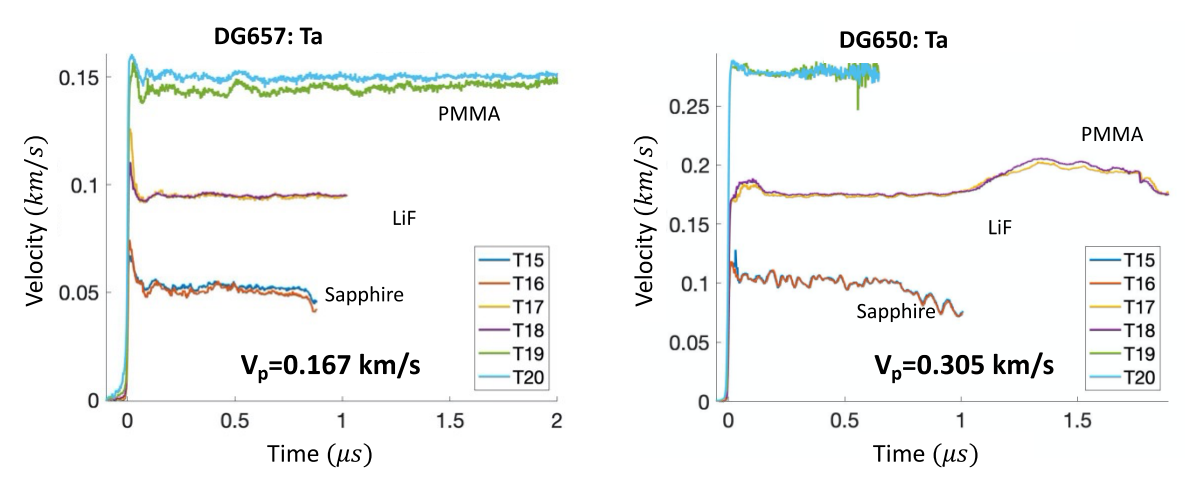


Figure 5. Velocity histories measured at the impactor/window interface for Ta deposited by controlled atmosphere plasma spray and impacted in a reverse-ballistic configuration at low (left) and high (right) impact velocities.

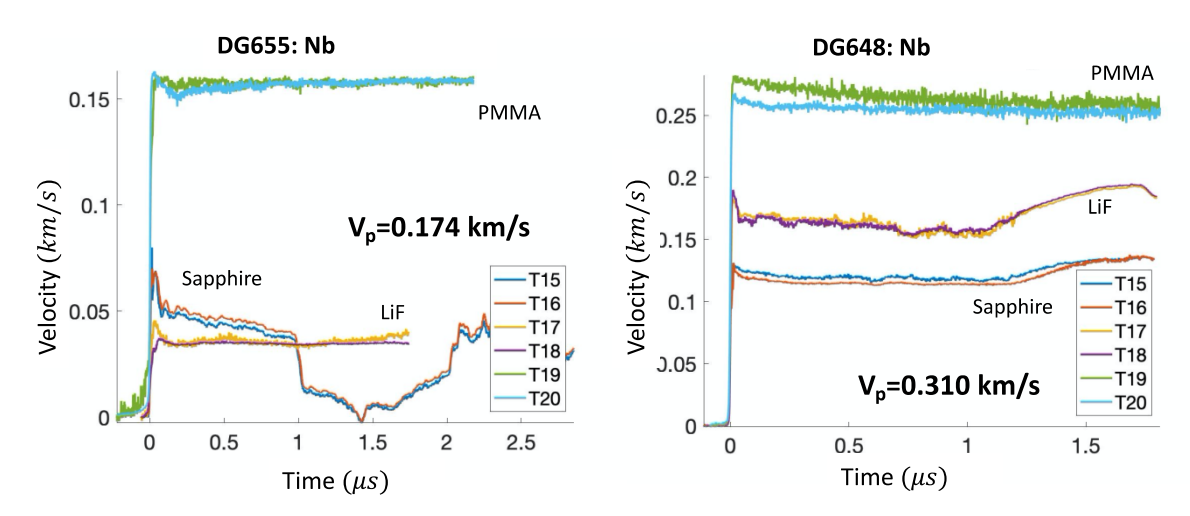


Figure 6. Velocity histories measured at the impactor/window interface for Nb deposited by controlled atmosphere plasma spray and impacted in a reverse-ballistic configuration at low (left) and high (right) impact velocities.

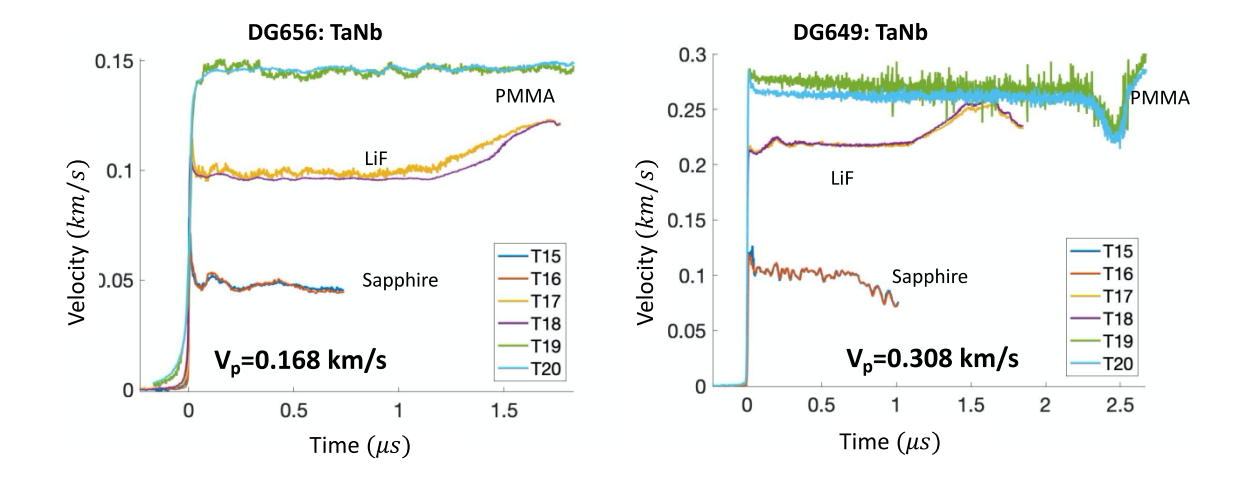


Figure 7. Velocity histories measured at the impactor/window interface for Ta/Nb blend deposited by controlled atmosphere plasma spray and impacted in a reverse-ballistic configuration at low (left) and high (right) impact velocities.

Table 4 summarizes the testing parameters for each shot. The measured interface velocity,  $u_{Avg}$ , in combination with the measured projectile velocity,  $u_0$ , and EOS (constants ( $c_{0,w}$  and  $S_w$ ) shown below Table 4) for each respective window at initial density,  $\rho_{0,w}$ , was used to determine the Hugoniot locus through impedance matching, where the shock velocity of the window  $U_{s,w}$  is equivalent to the wavespeed in the cold spray materials according to Equations 1-3:

$$u_p = u_0 - u_{Avg} \tag{1}$$

$$U_{s,w} = c_{0,w} + S_w u_{p,w} \tag{2}$$

$$\sigma_{Hug} = \rho_0 U_{s,w} u_p \tag{3}$$

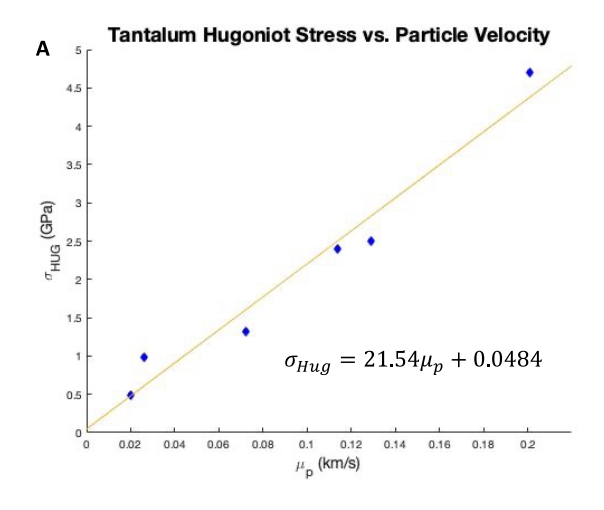
The resulting Hugoniot stress values,  $\sigma_{Hug}$  and the calculated compressive strain,  $\varepsilon_{Hug}$ , are shown in Table 4.

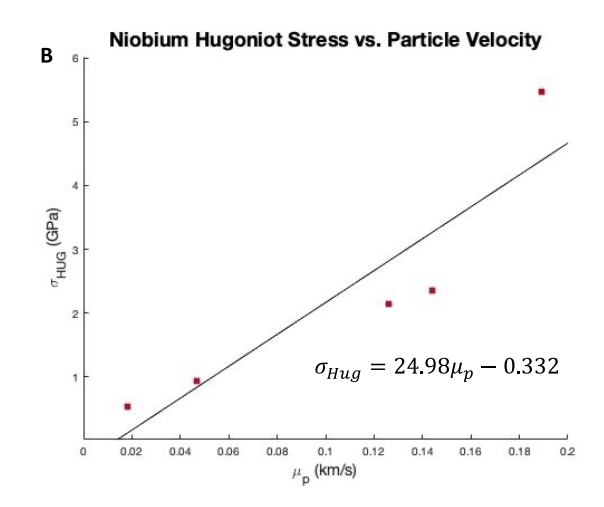
Table 4. Summary of measured projectile ( $u_0$ ), average interface velocity measured ( $u_{Avg}$ ), the particle velocity ( $u_p$ ), and the calculated Hugoniot stress ( $\sigma_{Hug}$ ) and strain ( $\varepsilon_{Hug}$ ) for Ta, Nb, and TaNb with initial density given ( $\rho_o$ ).

Shot #3	Sample/ Window Type	Window Thickness (mm)	Sample Density $ ho_0$ (g/cc)	Sample Thickness (mm)	Projectile Velocity u <sub>0</sub> (mm/μs)	Average Interface Velocity u <sub>Avg</sub> (mm/μs)	Effective Hugoniot Particle Velocity *u <sub>p</sub> (mm/μs)	Effective Hugoniot Stress σ <sub>Hug</sub> (GPa)	Effective Hugoniot Strain ε <sub>Hug</sub>
DG 648	Nb/PMMA	12.444±0.009	7.826 ±0.008	3.816±0.009	0.310±0.001	0.263±0.003	0.047±0.003	0.935±0.003	0.018±0.001
	Nb/LiF	12.001±0.003	-	-	-	0.166±0.003	0.144±0.003	2.352±0.003	0.069±0.002
	Nb/Sapphire	12.032±0.008	•	-	-	0.121±0.007	0.189±0.007	5.465±0.007	0.051±0.002
DG655	Nb/PMMA	12.469±0.011	7.826 ±0.008	3.963±0.006	0.174±0.001	0.156±0.002	0.018±0.002	0.525±0.002	0.005±0.001
	Nb/LiF	11.986±0.001	-	-	-	0.036±0.001	0.137±0.002	0.498±0.002	0.298±0.003
	Nb/Sapphire	12.107±0.011	-	-	-	0.048±0.005	0.126±0.005	2.151±0.003	0.058±0.002
DG649	TaNb/PMMA	12.403±0.011	11.854±0.114	3.327±0.010	0.308±0.001	0.263±0.003	0.045±0.003	0.935±0.002	0.026±0.002
	TaNb/LiF	11.999±0.006	-	-	-	0.218±0.005	0.090±0.005	3.127±0.003	0.031±0.002
	TaNb/Sapphire	12.060±0.003		-	-	0.151±0.003	0.157±0.003	6.830±0.007	0.043±0.001
DG656	TaNb/PMMA	12.200±0.017	11.854±0.114	3.233±0.011	0.168±0.001	0.146±0.002	0.022±0.002	0.487±0.003	0.012±0.001
	TaNb/LiF	12.021±0.003	-	-	-	0.098±0.002	0.070±0.002	1.367±0.003	0.042±0.001
	TaNb/Sapphire	12.016±0.003	-	-	-	0.048±0.004	0.120±0.005	2.171±0.007	0.078±0.003
DG650	Ta/PMMA	12.469±0.010	15.159±0.060	3.876±0.025	0.305±0.001	0.279±0.003	0.026±0.003	0.999±0.003	0.010±0.001
	Ta/LiF	11.952±0.002	-	-	-	0.176±0.005	0.129±0.005	2.501±0.003	0.101±0.004
	Ta/Sapphire	12.037±0.001	-	-	-	0.104±0.006	0.201±0.006	4.701±0.007	0.130±0.004
DG657	Ta/PMMA	12.155±0.018	15.159±0.060	4.075±0.030	0.167±0.001	0.147±0.002	0.020±0.002	0.493±0.003	0.012±0.001
	Ta/LiF	12.031±0.005	-	-	-	0.095±0.002	0.072±0.002	1.321±0.003	0.060±0.002
	Ta/Sapphire	11.916±0.004	-	=	=	0.053±0.004	0.114±0.004	2.391±0.007	0.082±0.003

\*LIF:  $\rho_0$ =2.640 g/cm³,  $c_0$ =5.148 km/s, S=1.353 \*PMMA:  $\rho_0$ =1.186 g/cm³,  $c_0$ =2.598 km/s, S=1.516 \*Sapphire:  $\rho_0$ =3.985 g/cm³,  $c_0$ =11.208 km/s, S=0.89

The measured Hugoniot states are plotted in the Hugoniot stress ( $\sigma_{Hug}$ )- particle velocity ( $u_p$ ) plane in Figure 8. Hugoniot stress as a function of shock-induced particle velocity for controlled atmosphere plasma spray-deposited materials with the linear Rankine-Hugoniot fit for Ta (A), Nb (B) and TaNb (C), respectively. A linear Rankine-Hugoniot fit to the data in this plane is designated for each material type. Although this is the standard method of reporting Hugoniot data, we note that due to the heterogeneity of CAPS materials this measurement is an effective Hugoniot state that may consist of a distribution of states that cannot be discreetly measured with VISAR.





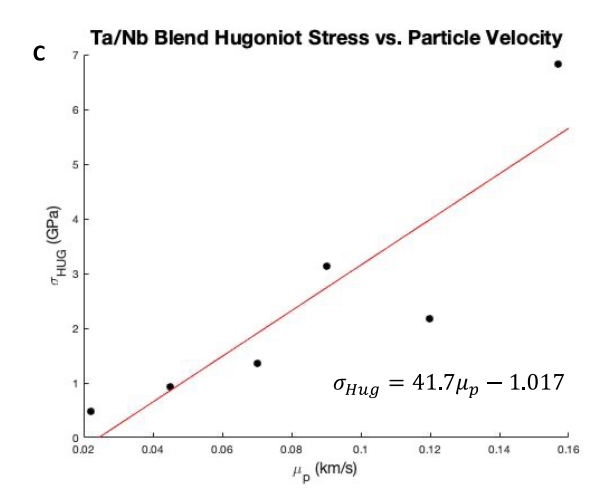


Figure 8. Hugoniot stress as a function of shock-induced particle velocity for controlled atmosphere plasma spray-deposited materials with the linear Rankine-Hugoniot fit for Ta (A), Nb (B) and TaNb (C), respectively.

The effect of deposition process of sprayed material for both Ta and Nb was compared to solid Hugoniot points reported previously by Marsh<sup>49</sup> in Figure 9A and B. Further, the Ta/Nb blend with varying spray techniques is also shown in Figure 9C. The Rankine-Hugoniot fit are quadratic or linear based on previous reports for Air spray and Cold Spray, respectively.<sup>31,37</sup> For the pure metals an overall trend in material stiffness indicated by the slope of the fit can be observed with the pure solid material having the highest stiffness compared to the CAPS deposited film, with the AS and CS falling in between. We note here, to have a quantitative understanding of the dependence of spray techniques in terms of Hugoniot fit and uncertainty, more data is needed on a larger sample subset for each spray technique, but from the fits shown below we attribute the differences in stiffness to the concentration of oxides forming during the respective spray process. The AS process have very little control of oxide formation due to the ambient atmosphere present during deposition resulting in a ceramic-like material that tends to be stiffer and more brittle. Whereas the CAPS material has inherently less oxide formation due to the controlled argon environment during deposition. Generally, TS deposition leads to inclusion of voids causing more ductility in the material and exhibiting more elastic behavior during compression compared to solid.

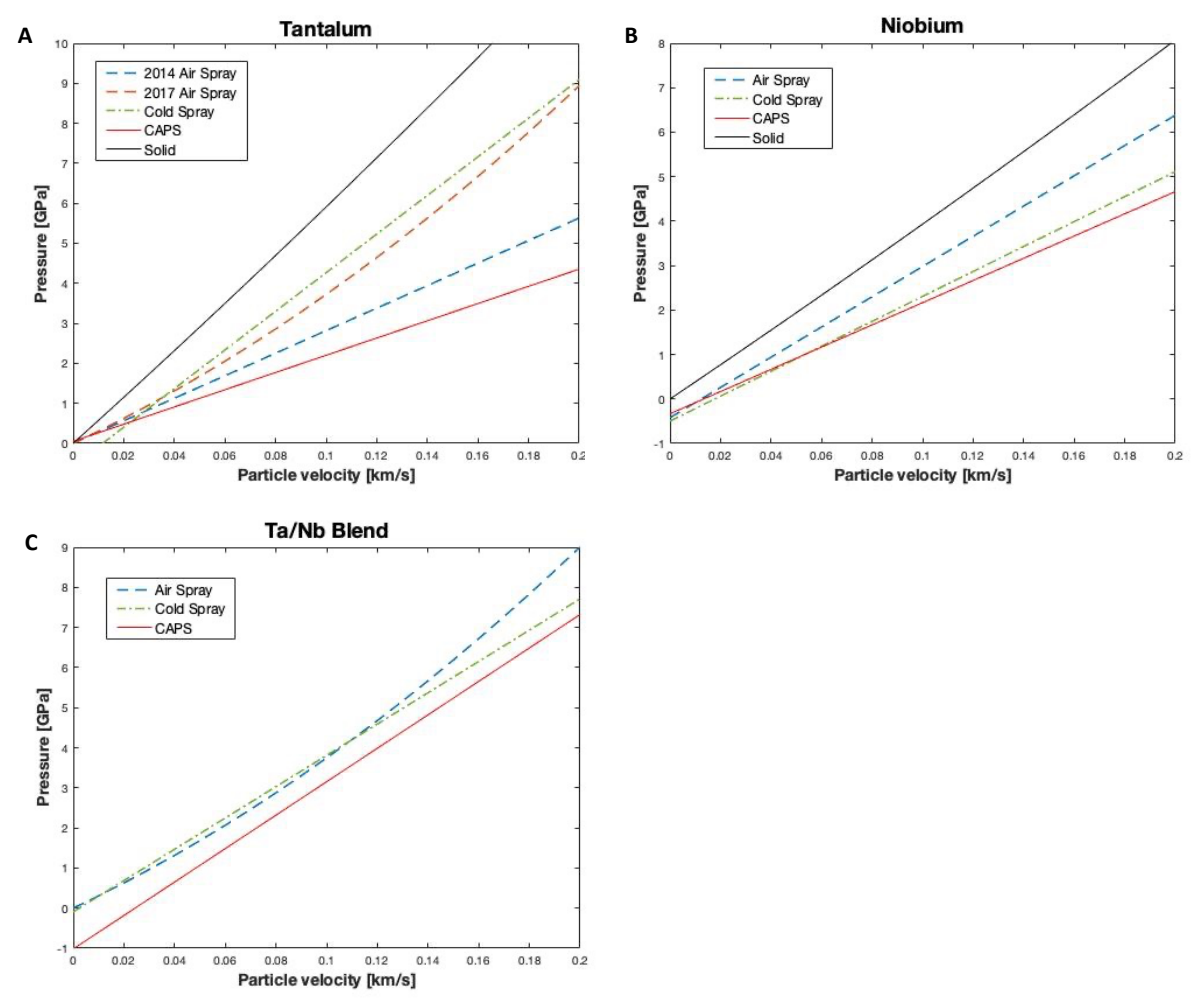


Figure 9. Hugoniot stress as a function of shock-induced particle velocity for air, cold, and controlled atmosphere spray-deposited materials for Ta, Nb and TaNb, respectively. For the pure Ta and Nb materials the solid Hugoniot is also shown.

Experiments to record an extended transmitted wave profile were conducted in the forward-ballistic configuration. In these experiments, all three samples were impacted by a c-cut sapphire impactor simultaneously, and the wave profile was observed at a sample-window interface. This configuration was used to allow for a longer diagnostic read time for comparison with simulations and to measure the Hugoniot Elastic Limit (HEL) and peak stress upon shock transmission into the sapphire window. Additionally, time of arrival probes were included in the target plate to allow for measurement of the wave speed. Sample, impactor, and window metrology is given in Table 5.

Table 5: Sample, impactor, and window metrology for transmitted wave shots.

Shot	Impactor Thickness [mm]	Sample	Thickness [mm]	Density [g/cm <sup>3</sup> ]	Window Thickness [mm]
		Та	1.217±0.003	15.39±0.23	11.999±0.003
		Nb	1.032±0.003	7.83±0.01	12.007±0.003
DG652	4.027±0.013	Ta/Nb	1.059±0.003	11.97±0.35	11.988±0.003
		Та	1.138±0.003	15.16±0.06	11.987±0.003
		Nb	1.164±0.003	7.82±0.01	11.987±0.003
DG653	4.027±0.003	Ta/Nb	1.205±0.003	11.85±0.12	11.989±0.003

VISAR data were recorded using Oz focusing probes on all samples. On all traces an initial increase in velocity to the HEL was observed followed by a short plateau and more gradual increase to the peak state. Window profiles for all samples are shown in Figure 10.

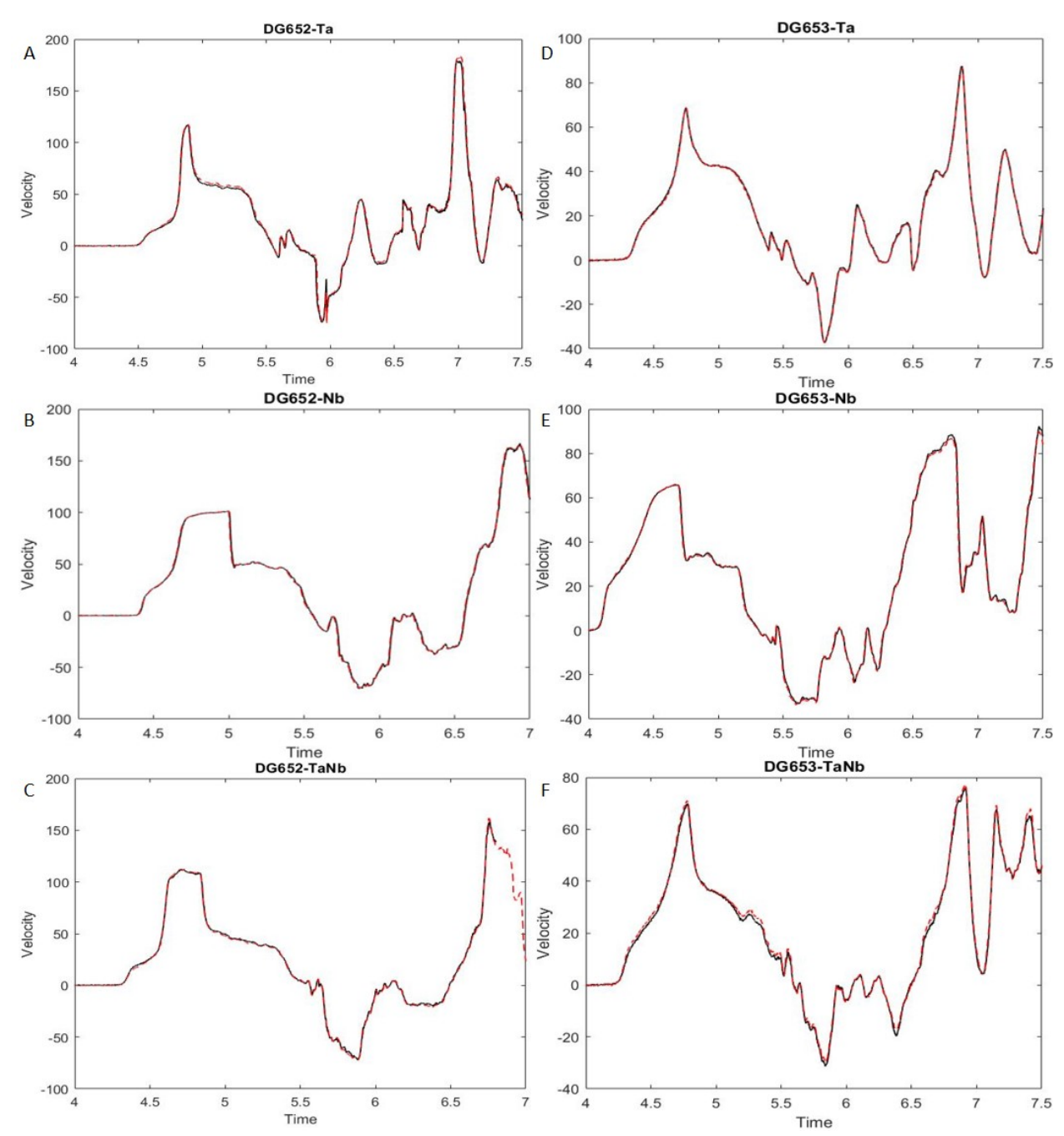


Figure 10: Wave profiles measured at sample-window interface for transmitted wave shots. HEL velocities were similar for both the higher velocity DG652 shot (left, panels A-C) and the lower velocity DG653 shot (right, panels D-F). Steady peak states were not observed for Ta on DG652 or Ta and TaNb on DG653.

The wave profiles exhibit significant temporal variation in the peak state, with no steady peak present in three of the six profiles. On both Ta samples (panels A and D), a slow rise to the HEL is observed, followed by an increase in velocity up to the peak state. The peak states in these experiments were short-lived and followed by a sudden drop in velocity to a steady state for  $>0.1~\mu s$ .

The TaNb sample on shot DG653 exhibited a similar behavior, however noticeable acceleration was identified in the quasi-steady state after the peak.

Both Nb samples and the TaNb sample on DG652 exhibited fast acceleration to the HEL followed by a slower ramp to the peak state. Additionally, these samples had noticeable temporal variation in the peak state or in a 50% peak state coinciding with arrival of the first tensile wave at the window. Variation in the wave profile is likely related to reverberations within the sample due to the stochastic microstructure. The more significant variation present in the TaNb peak state is also consistent with this hypothesis as local stresses will differ for Ta, Nb, and void within the sample. This behavior was also observed for both cold spray and air-plasma sprayed deposits.

The lack of a steady peak state for the Ta samples and one TaNb sample does not agree with the results of transmitted wave experiments on cold sprayed or air-plasma sprayed materials. In those experiments, a sharp rise to the HEL was followed by a gradual increase to a constant peak state prior to tension being induced in the sample. Possible causes for the sharp peak and immediate release are poor adhesion between the sample and window, damage to the sapphire impactor during flight, or significant wave reverberations in the sample. The latter option is the most likely as it would also explain the slower acceleration to the HEL if the pores within the CAPS material are more compressible. In this case, the shock in the sample would expend more energy compacting pores during transit and additional reverberations will devolve the shock at the window into a series of small perturbations which effectively drive ramp-wave compression in the sample. Post-mortem analysis of recovered material can be used to identify whether a significant decrease in porosity occurred during the experiment.

The peak stress and HEL stress was determined from a reflected Hugoniot approximation and impedance matching to the sapphire window. From the Hugoniot measurements discussed previously, we can determine the impedance matching to the sapphire window to convert the measured velocity and window pressure to an *in-situ* pressure in the sample. The impedance matching diagram for Ta is shown in Figure 11. The slope of the Ta Hugoniot is significantly lower than that of the sapphire window, so a strong reshock was driven into the Ta samples upon breakout into the sapphire window; similar relative slopes were identified for both the Nb and TaNb. The elastic wave speed was determined from transit times from the tilt-corrected impact on the sample to breakout into the sapphire window. Elastic shock velocities ( $U_S^{el}$ ), peak stress ( $\sigma$ ), and HEL, are given in Table 6.

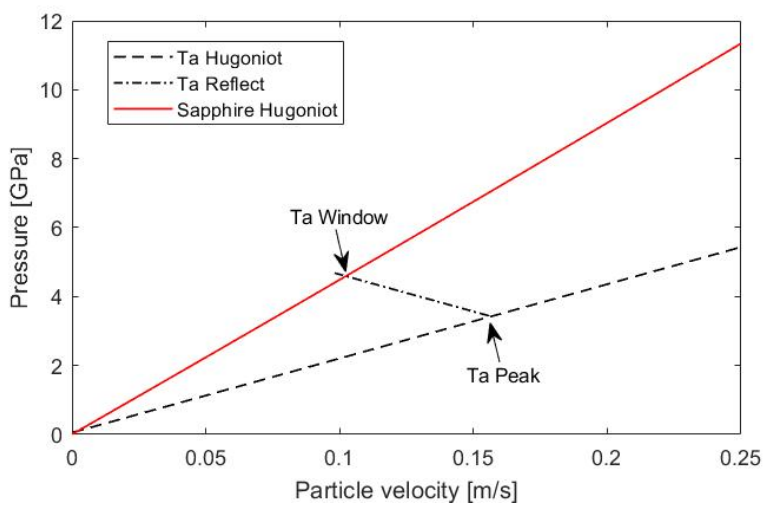


Figure 11: Impedance matching diagram for CAPS tantalum samples on transmitted wave shots. The sapphire window is higher impedance than the sample and a reshock is reflected back into the material.

Table 6: Impact velocity, elastic wavespeed, peak stress, and Hugoniot elastic limit for samples on transmitted wave shots.

Shot	Impact velocity [mm/µs]	Sample	Transit time [µs]	$U^{el}_{\mathcal{S}}$ [mm/ $\mu$ s]	σ [GPa]	HEL [GPa]				
		Та	0.393±0.016	3.10±0.16	3.91±0.13	$0.44\pm0.13$				
DG652	0.231±0.001	Nb	0.298±0.012	3.46±0.17	3.31±0.15	$0.56\pm0.14$				
						Ta/Nb	0.314±0.013	3.37±0.17	4.20±0.18	0.23±0.17
		Та	0.372±0.015	3.06±0.12	2.30±0.14	$0.58\pm0.14$				
DG653	653 0.170±0.001	Nb	0.350±0.014	3.33±0.13	2.12±0.13	$0.52 \pm 0.14$				
		Ta/Nb	0.415±0.017	2.91±0.12	2.52±0.17	0.12±0.13				

Elastic shock velocities on both shots were similar to the longitudinal sound velocity in the material. This is expected as the peak stress was only slightly above the HEL, and minimal compression would have been induced by the shock. The elastic velocities and HEL for the Ta and Nb samples were consistent between both shots, whereas the blend material has a significant difference in sound velocity. The HEL for the blend is significantly lower than either single material, and its uncertainty is sufficient to include zero HEL for shot DG653. The large uncertainty is an artifact of the assumed 10% of a fringe systematic error in VISAR, as the matching between the two traces supports uncertainty ~½ the quoted value. The difference in HEL between the blend and single materials warrants further investigation.

Forward-ballistic spall experiments were conducted to obtain transmitted wave profiles during tensile loading of free-standing CAPS samples. These experiments differed from the transmitted wave experiments described previously by measuring a free-surface velocity rather than window interface velocity. In the absence of full compaction, comparison between the windowed and free-surface measurement provide bounding of the true HEL as a reflected Hugoniot approximation will

introduce systematic error for porous material. The free-surface measurement also enables sample recovery for post-mortem fracture analysis which will be described below. The velocity histories show a sharply rising elastic precursor wave followed by a non-steady, dissipative plastic wave as indicated by the circle for each sample type. The measured free-surface precursor amplitude, the corresponding in-situ particle velocity behind the incident elastic wavefront and the HEL for each experiment is reported in

Table 7.

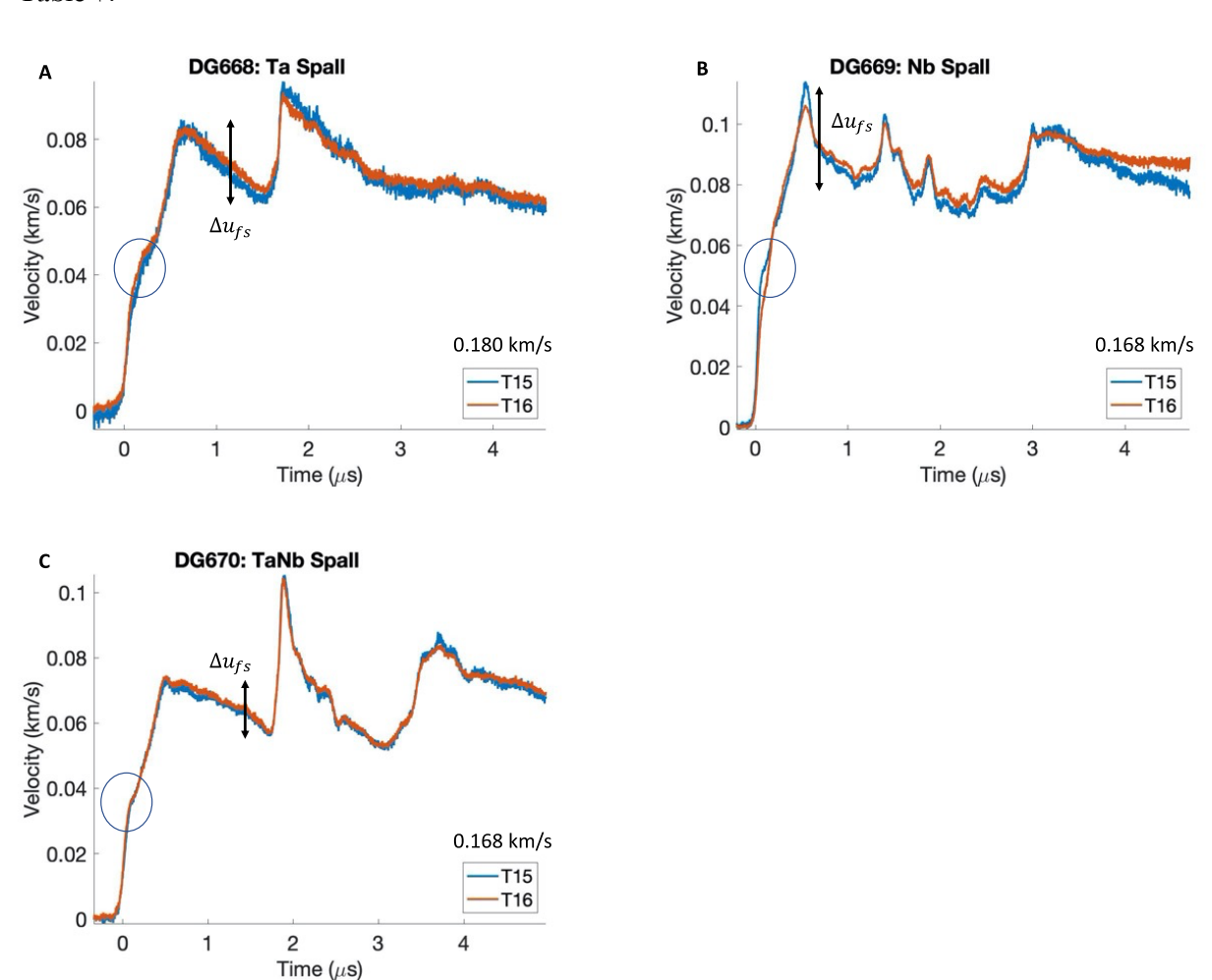


Figure 12. Free-surface velocity histories measured for cold spray-deposited samples subjected to a sapphire impact at the specified velocities. Circle indicates the transition from elastic to plastic deformation.

Table 7. Hugoniot elastic limit stress, pressure, yield strength and shear stress are shown for CAPS materials.

Shot #	Sample Type	Sample Thickness (mm)	Projectile Velocity (km/s)	u <sub>fse</sub> HEL (km/s)	σ HEL (GPa)	Pressure HEL (GPa)	HEL Yield Strength (GPa)	HEL Shear Stress (GPa)
DG668	Ta	3.097±0.005	0.180±0.003	0.046±0.002	0.555	0.368	0.280	0.140
DG669	Nb	3.679±0.007	0.168±0.002	0.050±0.002	0.559	0.371	0.282	0.141
DG670	TaNb	3.229±0.010	0.168±0.001	0.036±0.001	0.481	0.319	0.243	0.121

After the Hugoniot Elastic Limit is reached a non-constant response upon reaching the peak stress state is suggestive of a non-uniform plastic deformation. The non-steady decay in the plastic wave is observed for all materials and is consistent with the forward-ballistic experiments described above for a sapphire window impacted by CAPS-deposited material at approximately the same velocity. Dispersion of the plastic wave front occurs with the slight decrease in velocity but the characteristic "pull-back" signal is observed, where the free surface velocity drops after the peak velocity and returns to a second peak state. The tensile stress just before spall fracture occurs is known as the spall strength and can be approximated by the velocity-pullback ( $\Delta u_{fs}$ ) seen in the velocity traces shown previously, sound velocity ( $C_0$ ) and the initial density ( $\rho_0$ ) according to the approximation below. The calculated spall strengths resulting from the three experiments are shown in Table 8.

$$\sigma_{sp} = \frac{1}{2} \rho_o C_o \Delta u_{fs}$$

Table 8. Peak free surface velocity  $(u_{fs})$ , pullback velocity  $(\Delta u_{fs})$ , and calculated spall strength  $(\sigma_{sp})$  for CAPS samples.

Shot #	Sample Type	Projectile Velocity (km/s)	$u_{fs}$ Free Surface Velocity (km/s)	$\Delta u_{fs}$ Velocity Pull-back (km/s)	$\sigma_{sp}$ Spall Strength (GPa)
DG668	Ta	0.180±0.003	0.084±0.001	0.066±0.001	0.216±0.003
DG669	Nb	0.168±0.002	0.107±0.001	0.083±0.001	0.276±0.005
DG670	TaNb	0.168±0.001	0.073±0.001	0.057±0.001	0.205±0.003

The recovered spall samples were examined to determine the extent of fracture and understand fracture mechanisms within the sample. Of the three materials, only the Ta sample was not recovered intact, and was instead recovered in four large fragments. A fifth fragment from the 6061-Al target plate was also recovered. This fragment sheared off the target plate due to the sample becoming wedged within the plate rather than separating cleanly during the experiment. As such, it cannot be conclusively determined whether the fracture occurred because of spallation due to tension from the rarefaction waves or shear from the target plate. Because the other samples were recovered intact and showed signs of spall in the wave profile, the most likely scenario is that the Ta sample had spall planes form during tension, which formed weak spots that then fractured due to shear forces.

The Ta fracture surface was examined by high-resolution scanning electron microscopy (SEM) with a JEOL NeoScope JCM-7000 benchtop SEM which was recently acquired at the DICE facility. The DICE SEM uses a tungsten filament and has both backscattered electron and secondary electron detectors with magnification capabilities up to  $100,000\times$ . It also has energy dispersive spectroscopy (EDS) built-in to identify material compositions in the examined sample. Fracture surface imaging is typically done using secondary electron imaging because the pseudo-3D images provide the most detail of height variation on the surface. <sup>50</sup> Conversely, backscattered electron images are more sensitive to different materials, but lack the height information. The secondary electron images were also used to examine fracture surfaces for previous studies of solid or TS tantalum. <sup>35,51,52</sup>

Images of the tantalum fracture surface were taken at magnifications of  $100 \times (250 \text{ nm/px})$ ,  $1000 \times (25 \text{ nm/px})$  and  $2000 \times (12.5 \text{ nm/px})$ . In the lowest resolution image (Figure 13), a single large spall plane is present through the center of the sample. The resolution of the picture is insufficient to make a clear determination of whether brittle or ductile fracture occurred in the sample. The spall plane generally follows splat boundaries, which agrees with the previous results on CS and AS samples. The size of the plane is indicative of complete or near-complete spall, but determination of whether it occurred during the shot or due to tensile loading on an incipient spall surface when being removed from the target plate is impossible. In addition to the large spall plane, voids where adjacent splats appear to have pulled apart from one another are present in the image. The irregular deformation of the surface precludes further investigation of the spall plane, and further investigation is warranted.

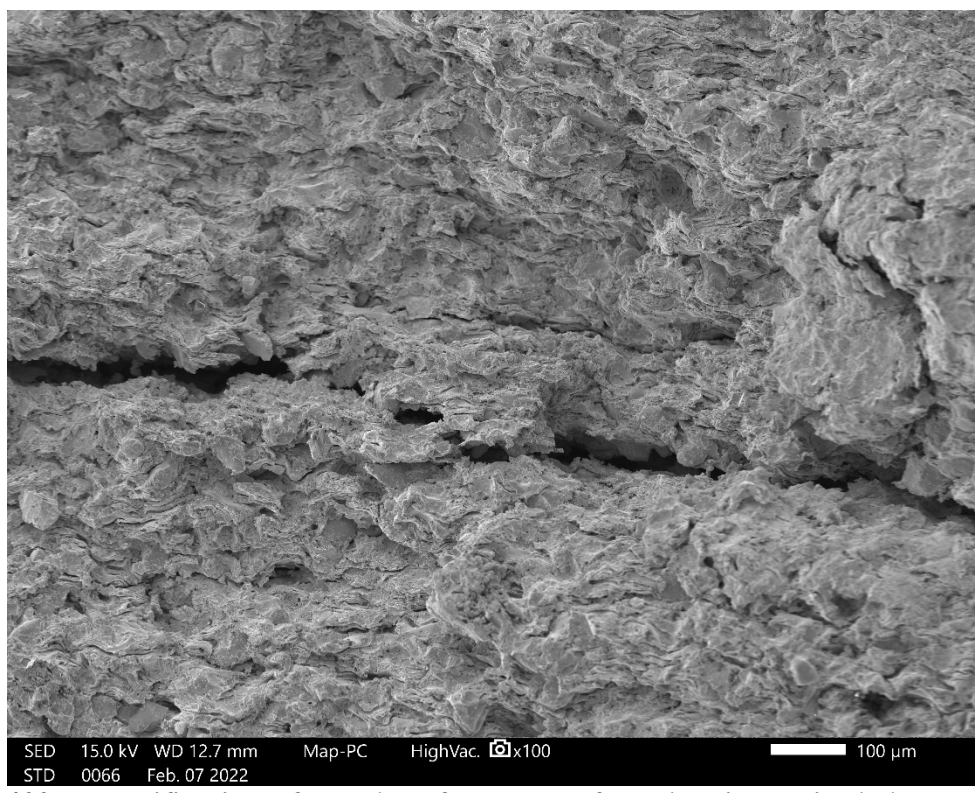


Figure 13: 100x magnification of tantalum fracture surface showing a single large spall plane through the center of the image.

At higher resolution (Figure 14), the fracture surface shows a highly irregular texture, which is more indicative of ductile fracture. The retention of ductility in the CAPS Ta sample strongly supports the results from the spall strength experiments where the CAPS materials were found to have measurable spall strength. This contrasts with the earlier work on AS and CS materials where fracture was found to be largely brittle, and no measurable spall strength could be identified. Large smooth surfaces are present where the fracture occurred as a brittle failure along splat boundaries. In between locations where fracture occurred along the splat boundaries, a series of irregular surfaces are present. In particular, void nucleation sites and risers can be identified on sharp ridges where the fracture surface traversed a splat and plastically deformed the material prior to failure. Deformation features are predominantly in the direction of the impact and tensile strain. However, because shear forces from separation from the target plate would also induce forces in the same direction the cause of the fracture is inconclusive from the SEM images. The presence of increased ductile fracture and fewer fractures along splat boundaries when compared to the AS or CS samples indicates that intersplat adhesion is enhanced for samples fabricated using the CAPS process.

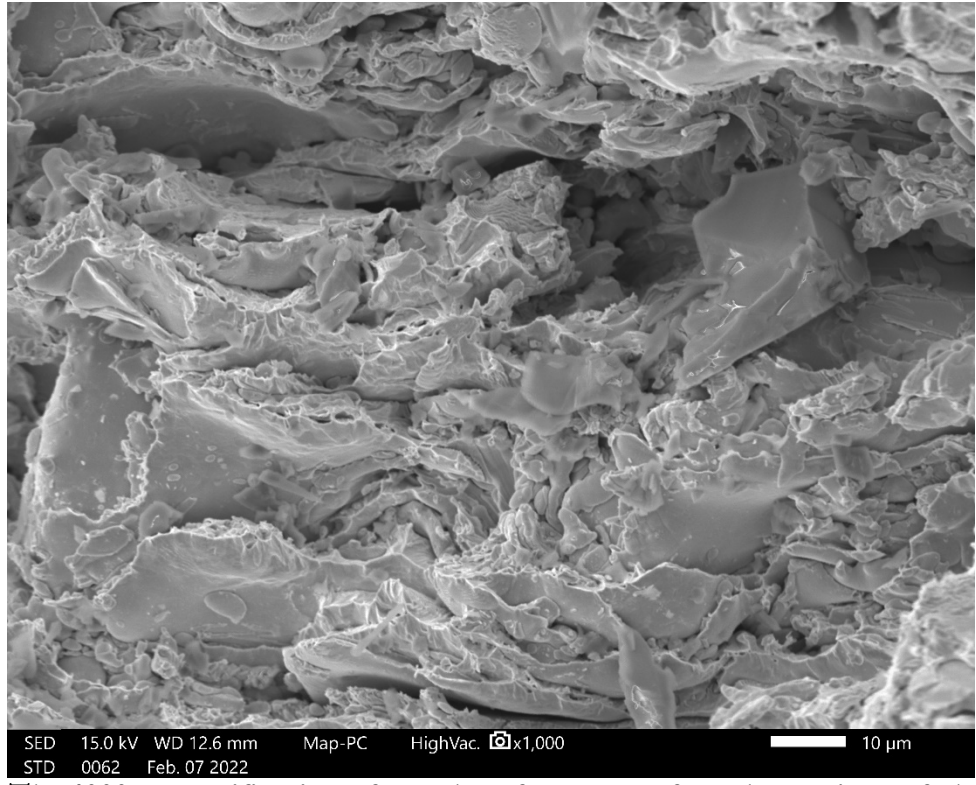


Figure 14: The 1000x magnification of tantalum fracture surface shows signs of plastic deformation between locations where fracture followed splat boundaries.

## Cross-sectioning and imaging

The recovered Nb and TaNb blend samples were cross-sectioned and imaged on the DICE SEM. To get a better-quality image, after cross-sectioning, hand polishing was carried out to remove roughness contributed by the diamond saw. The samples were polished to surface roughness on the order of tens of microns prior to imaging.

Images of the cross-sectioned samples were taken at 30-4500× magnification to allow for observation of the broader spall plane and features within the plane. In both cases, complete spall and fracture did not occur so the imaging was focused within the largest observed voids. High resolution imaging of the inside of a spall void is able to provide insight into the mechanism that induced failure within the material. In cases where fracture has not yet occurred, the amount of information on ductile vs brittle behavior which can be gleaned is limited, however some detail on the material properties is possible

#### Niobium

The Nb sample experienced incipient spall as a result of the experiment. When looking at the low (37x) magnification image of the sample shown in Figure 15, there is a defined spall plane with width ~2 mm to which the damage is localized. The fracture sites are indicative of incipient spall rather than complete spall as they have not coalesced into a full plane which could cause fracture of the sample. However, the size of the fracture sites are tens of microns across and there are a significant number of locations where multiple voids have coalesced into larger damage sites. This indicates that the amount of tension induced in the sample was sufficient to not only nucleate voids and cause incipient spall, but that it was also able to induce growth of the nucleated sites. On this

shot, the peak stress was 2.35 GPa whereas the measured spall strength was 0.276 GPa. The amount of observed growth is expected for total tensile forces near that where complete failure would occur. The peak stress where the sample would be expected to transition from incipient to complete spall is likely <25% greater than that achieved in this work. The fact that the material did not fracture completely even though the peak stress was >8× larger than the spall strength is interesting. What it could indicate is that the high ductility in the CAPS material and pre-formed voids from the spray process enable tensile strain release due to wave reverberations or deformation and compression of existing voids. The extremely low Poisson's ratio may also contribute as it would imply less contraction due to tension than in other materials. Further study into damage mechanisms in CAPS materials is warranted as it could provide insight into future material design options.

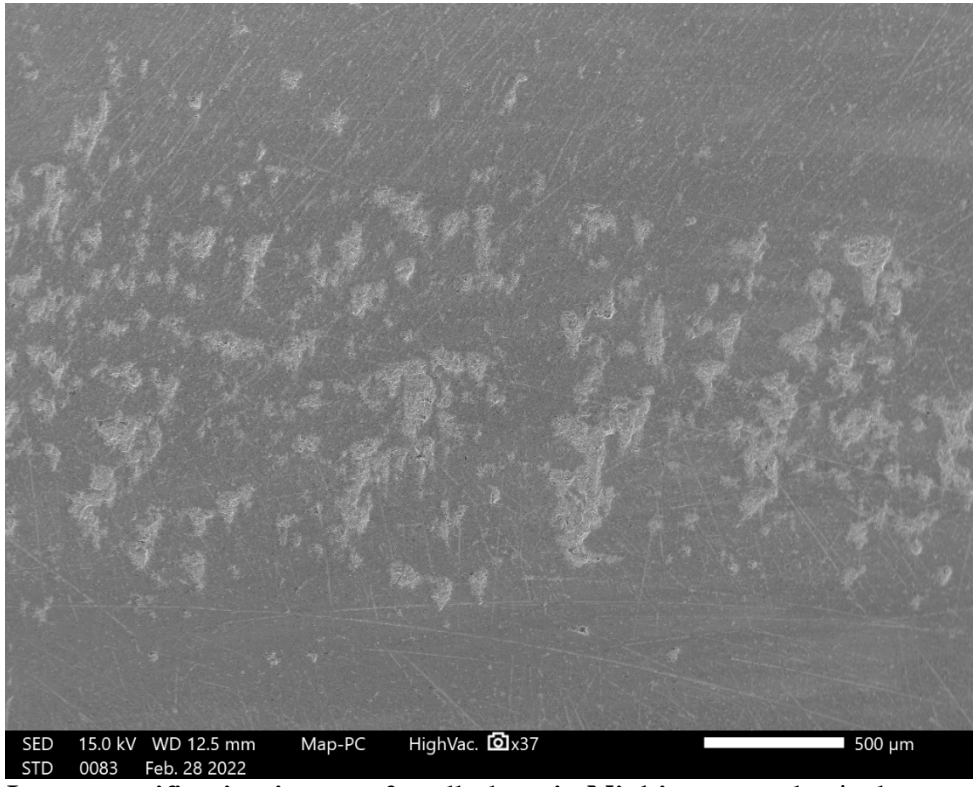


Figure 15: Low-magnification image of spall plane in Niobium sample. A clear spall plane is present, however the damage sites have not coalesced and induced complete spall.

At high (1300×) resolution, a clear damage site can be observed following a splat boundary in Figure 16. This behavior would be expected for these materials due to the nature of fabrication. Similar to air spray or cold spray materials, the movement of the nozzle is rasterized over the substrate being sprayed. As a result, when a splat is deposited onto a given location, it typically has weaker bonding to the previous layer than it does to material within itself. Other damage in the image shows signs of force in its vertical direction. This orientation corresponds with the tensile loading from the experiment, which supports a determination of ductility within the sprayed niobium sample. Such a determination is also supported by the presence of many sharp and irregular features, which are not typically observed in brittle materials. Hence, similar to the tantalum discussed above, the CAPS niobium has significantly higher ductility than either AS or CS materials and recovers more of the properties of the base material.

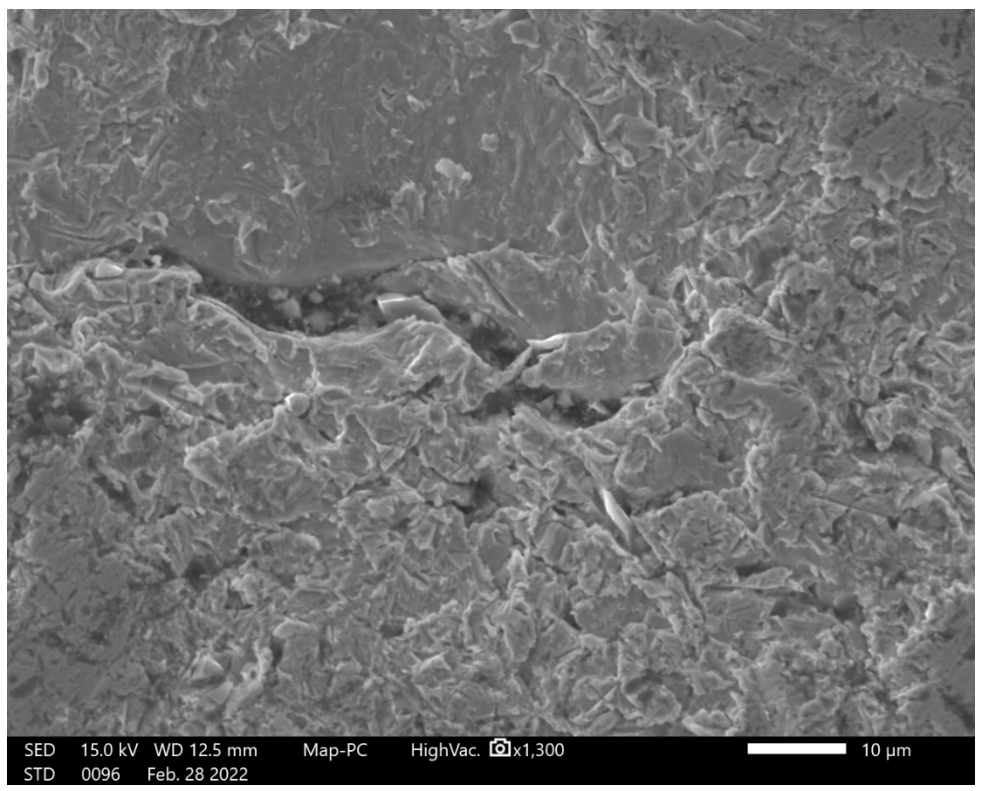


Figure 16: 1300x magnification image of nucleated void in niobium.

#### Tantalum-niobium blend

The spall plane in the Ta-Nb blend is more pronounced when compared with the pure Nb sample. In the low  $(30\times)$  resolution image (Figure 17), a discrete band  $\sim$ 1.5 mm wide of damage sites is present across the entire sample. The size of the initial nucleated sites appears to be similar to that of the Nb sample, but the vast majority of the area is filled by sites where growth and coalescence has occurred. On the left-hand-side of the image, the damage sites have coalesced into a large fracture surface  $\sim$ 1.5 mm long  $\times$   $\sim$ 1 mm wide. Here we define "long" as being in the direction of the quasiuniaxial strain induced by the shock and tension. Similarly, the right-hand-side has a large region of coalescence where the voids have merged into the center where a complete spall plane would be expected to form. The degree of coalescence indicates that the sample is approximately at the transition from incipient to complete spall, and complete spall would occur with lower increased stress than required for the pure niobium. Similarly to the pure Nb, the peak stress should be sufficient to fully spall the sample, however the negative Poisson ratio and pre-formed voids may effectively damp the tensile force and prevent complete spall at these stresses.

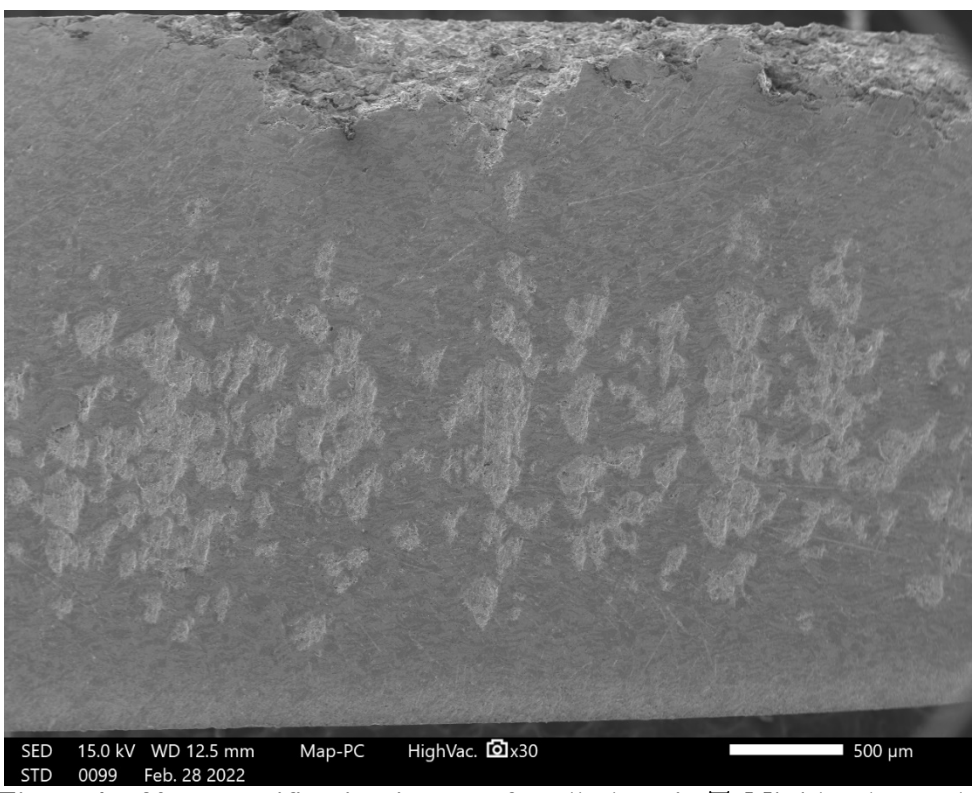


Figure 17: 30× magnification image of spall plane in TaNb blend sample

At high (1000×) magnification, imaging of the damage sites show larger voids and cracks running through the width of the sample. The presence of long interconnecting cracks which were not present in the pure niobium is a strong indicator to reinforce the hypothesis that the amount of increased yield required to induce complete spall is lower for the TaNb blend than for the pure material. An example of this is shown in Figure 18. The crack present in the center of the image both follows splat boundaries, but also traverses a Nb splat. Additional locations had longer cracks which connected individual damage sites together. The pattern of deformation is also indicative of ductile fracture within the material combined with the brittle behavior at splat boundaries. This, when combined with the results of the pure materials, demonstrates the increased robustness of the CAPS materials over other spray processes.

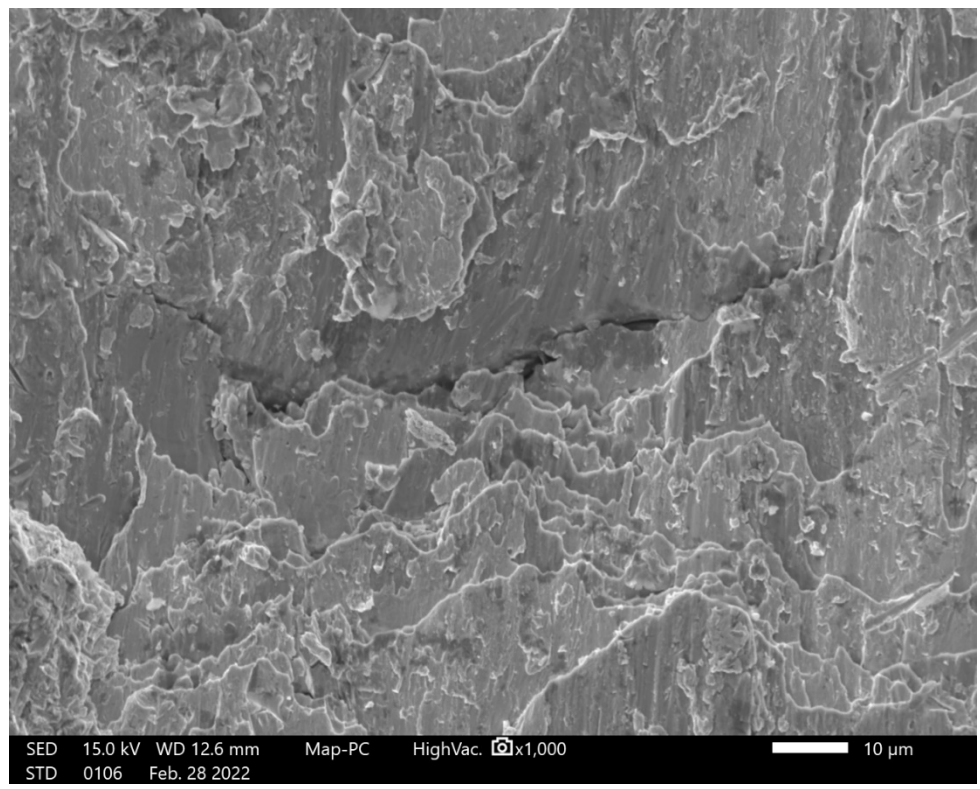


Figure 18: 1000× image of crack in damage site of Ta-Nb blend sample.

### Comparison between spray processes

Previously, we showed that AS and CS samples primarily failed due to brittle fracture,<sup>31,51</sup> and limited pockets of plastic deformation and ductile fracture existed in the recovered samples. The CAPS deposits on the other hand, show fracture surfaces with irregular texture, which is more indicative of ductile fracture. The retention of ductility allowed for the signature pull-back signal to be measured and a spall strength to be calculated for CAPS materials. This contrasts with the earlier work on AS and CS materials where no measurable spall strength could be identified.

The increased ductility of the CAPS materials corresponds with the softer response when compared to the CS and AS material which is likely due to the work hardening that arises during material deposition. In the event of lower oxide content, the properties of the pure metals can dominate the mechanical response rather than having a combined oxide-metal response. The high oxide content in the AS material effectively made it behave most similarly to a sintered or hot isostatic pressed ceramic where there was little bonding between particles when exposed to large tensile forces. The CS material had the highest density and lowest porosity but had reduced oxide content when compared to the AS material. This is mirrored in the HEL where the CS has HEL intermediate to the CAPS and solid, but the AS has negligible HEL due to instantaneous yielding and a stiff response dominated by compressive fracture. Hence, the CAPS process would be considered the most favorable option for materials which require tensile strength and the ability to support deformation without fracturing.

#### **CONCLUSIONS**

Shock loading experiments were conducted to probe the dynamic mechanical behavior of CAPS deposited materials with compositions of Ta, Nb and TaNb blend. The measured Hugoniot states for impact stresses ranging from 0.5-6.8 GPa are reported. Spall experiments were conducted to measure the transmitted wave profile and the respective Hugoniot Elastic Limit resulting from impact velocities of 0.168-0.231 km/s. Scanning electron microscopy was performed on the recovered spall samples and the fracture surfaces in CAPS Ta, Nb, and TaNb blend show similar characteristics which can be inferred to be representative of the general behavior of CAPS materials under dynamic loading. The difference in fragmentation behavior between Ta and the other samples may warrant more investigation into the spallation of these samples since we cannot conclude if tension due to spall or shear forces resulting from the momentum of the target plate caused failure. The CAPS samples primarily failed due to ductile fracture, with the Nb containing deposits showing insipient spallation. This compares to previous work on AS and CS materials that were primarily more brittle and showed no measurable spall strength.

#### **REFERENCES**

- A. Denoirjean, O. Lagnoux, P. Fauchais, and V. Sember, in Oxidation control in atmospheric plasma spraying: Comparison between Ar/H2/He and Ar/H2 mixtures, Nice, France, 1998, p. 809.
- G. Mauer, R. Vassen, and D. Stover, Surface & Coatings Technology **201**, 4796 (2007).
- P. Scardi, M. Leoni, L. Bertamini, and M. Marchese, Surface & Coatings Technology **86,** 109 (1996).
- M. Vaezi, P. Drescher, and H. Seitz, Materials 13 (2020).
- R. N. Raoelison, Y. Xie, T. Sapanathan, M. P. Planche, R. Kromer, S. Costil, and C. Langlade, Additive Manufacturing **19**, 134 (2018).
- S. Beauvais, V. Guipont, F. Borit, M. Jeandin, M. Espanol, K. A. Khor, A. Robisson, and R. Saenger, Surface & Coatings Technology **183**, 204 (2004).
- <sup>7</sup> C. I. Sarafoglou, D. I. Pantelis, S. Beauvais, and M. Jeandin, Surface & Coatings Technology **202**, 155 (2007).
- A. Y. Klimenko and R. W. Bilger, Progress in Energy and Combustion Science **25**, 595 (1999).
- S. E. Pratsinis, Progress in Energy and Combustion Science **24**, 197 (1998).
- W. Y. Li, K. Yang, S. Yin, X. W. Yang, Y. X. Xu, and R. Lupoi, Journal of Materials Science & Technology **34**, 440 (2018).
- P. Fauchais and M. Vardelle, Pure and Applied Chemistry **66**, 1247 (1994).
- T. H. Van Steenkiste, J. R. Smith, R. E. Teets, J. J. Moleski, D. W. Gorkiewicz, R. P. Tison, D. R. Marantz, K. A. Kowalsky, W. L. Riggs, P. H. Zajchowski, B. Pilsner, R. C. McCune, and K. J. Barnett, Surface & Coatings Technology 111, 62 (1999).
- M. F. Morks, Y. Tsunekawa, M. Okumiya, and M. A. Shoeib, Journal of Thermal Spray Technology **12**, 282 (2003).
- J. T. Mahaffey, A. W. Vackel, and A. Kustas, "Properties of Cold Sprayed and Controlled Atmospheric Plasma Sprayed High Entropy Alloy (CoCrFeMnNi) Coatings," (2021).
- S. Som, A. I. Ramirez, D. E. Longman, and S. K. Aggarwal, Fuel **90**, 1267 (2011).
- D. F. Susan, R. A. Kellogg, A. W. Vackel, J. Carroll, H. T., B. Salzbrenner, B. Mckenzie, D. E. Beatty, and P. Sarobol, "Microstructure and Properties of Cold-Sprayed Iron Coatings.," (2020).
- A. W. Vackel, E. Peleg, J. Varga, M. A. Blea-Kirby, C. Schmidt, and E. Gildersleeve, "Elastic measurements of plasma spray refractory metal coatings using thermal cycling of bi-layered beams," (2022).
- A. W. Vackel, J. T. Mahaffey, and P. Sarobol, "Aerosol Deposition and characterization of BaTiO3 films.," (2019).
- S. I. Imbriglio, M. Hassani-Gangaraj, D. Veysset, M. Aghasibeig, R. Gauvin, K. A. Nelson, C. A. Schuh, and R. R. Chromik, Surface & Coatings Technology **361**, 403 (2019).
- Z. P. Zhao, N. U. Tariq, J. R. Tang, Y. P. Ren, H. H. Liu, M. Tong, L. S. Yin, H. Du, J. Q. Wang, and T. Y. Xiong, Materials Science and Engineering a-Structural Materials Properties Microstructure and Processing 775 (2020).
- N. B. Maledi, O. P. Oladijo, I. Botef, T. P. Ntsoane, A. Madiseng, and L. Moloisane, Surface & Coatings Technology **318**, 106 (2017).
- D. M. Jafarlou, C. Walde, V. K. Champagne, S. Krishnamurty, and I. R. Grosse, Materials & Design **155**, 134 (2018).
- J. R. Tang, Z. P. Zhao, N. Li, X. Qiu, Y. F. Shen, X. Y. Cui, H. Du, J. Q. Wang, and T. Y. Xiong, Surface & Coatings Technology **377** (2019).

- K. E. Machethe, A. P. I. Popoolab, D. I. Adebiyi, and O. S. I. Fayomi, in *International Conference on Sustainable Materials Processing and Manufacturing*; Vol. 7, edited by T. C. Jen, W. Chiu, E. Akinlabi, and H. S. Chen (2016), p. 549.
- P. Cavaliere and A. Silvello, Surface Engineering **32**, 670 (2016).
- T. J. Flanagan, B. A. Bedard, A. M. Dongare, H. D. Brody, A. Nardi, V. K. Champagne, M. Aindow, and S. W. Lee, Scripta Materialia 171, 52 (2019).
- A. Moridi, S. M. Hassani-Gangaraj, S. Vezzu, L. Trsko, and M. Guagliano, Surface & Coatings Technology **283**, 247 (2015).
- A. Silvello, P. Cavaliere, A. Rizzo, D. Valerini, S. D. Parras, and I. G. Cano, Journal of Thermal Spray Technology **28**, 930 (2019).
- S. K. Shaha, S. B. Dayani, and H. Jahed, in *12th International Fatigue Congress*; Vol. 165, edited by G. Henaff (2018).
- N. W. Moore, Chantler, G.R., Vackel, A., Wise, J.L., Pokharel, R., Brown, D., SAND 2019-10376 (2019).
- B. A. Branch, C. A. McCoy, and A. W. Vackel, "Impact Response of Cold Spray Deposited Materials.," (2020).
- C. A. McCoy, B. A. Branch, and A. W. Vackel, "Transmitted wave measurements in cold sprayed materials under dynamic compression," (2021).
- J. M. Brown and J. W. Shaner, in *Shock Waves in Condensed Matter 1983*, edited by J. R. Asay, R. A. Graham, and G. K. Straub (Elsevier, Amsterdam, 1984), p. 91.
- <sup>34</sup> C. Dai, J. Hu, and H. Tan, Journal of Applied Physics **106**, 043519 (2009).
- D. R. Jones, S. J. Fensin, B. G. Ndefru, D. T. Martinez, C. P. Trujillo, and G. T. GrayIII, Journal of Applied Physics **124**, 225902 (2018).
- <sup>36</sup> A. C. Mitchell and W. J. Nellis, J. Appl. Phys. **52**, 3363 (1981).
- N. W. Moore, G. R. Chantler, A. Vackel, J. L. Wise, R. Pokharel, and D. Brown, "Stochastic shock observations from plate impact of porous refractory metals," Report No. SAND2019-10376 (2019).
- S. V. Razorenov, G. I. Kanel', G. V. Garkushin, and O. N. Ignatova, Physics of the Solid State **54**, 790 (2012).
- D. Rowe, in *Heat Treating Progress* (ASM International, 2003).
- S. M. Cardonne, P. Kumar, C. A. Michaluk, and H. D. Schwartz, International Journal of Refractory Metals and Hard Materials **13,** 187 (1995).
- A. W. Vackel and M. R. Kracum, "Controlled Atmosphere Plasma Spray Development Efforts for FY20," (2021).
- A. W. Vackel, "FY21 Thermal Spray Materials: Material Processing, Microstructural Characterization, and Thermo-Physical & Mechanical Properties," (2021).
- B. A. Branch, C. A. McCoy, and A. W. Vackel, "Impact Response of Cold Spray Deposited Materials," (2021).
- L. M. Barker and R. E. Hollenbach, Journal of Applied Physics 41, 4208 (1970).
- B. M. LaLone, O. V. Fat'yanov, J. R. Asay, and Y. M. Gupta, Journal of Applied Physics **103** (2008).
- S. C. Jones, M. C. Robinson, and Y. M. Gupta, Journal of Applied Physics 93, 1023 (2003).
- L. M. Barker and R. E. Hollenbach, Journal of Applied Physics **43**, 4669 (1972).
- A. W. Vackel and e. al., "FY21 Thermal Spray Materials: Material Processing, Microstructural Characterization, and Thermophysical and Mechanical Properties," (2021).
- S. P. Marsh, "LASL shock Hugoniot data," (1980).
- W. T. Becker, "Ductile and Brittle Fracture," (1992).

- N. W. Moore, C. A. McCoy, D. Dolan, B. Fox, A. Vackel, R. Hohlfelder, G. R. Chantler, C. Ball, D. Frayer, and M. Kaufmann, "Experimental Platforms for Thermomechanical Shock in Advanced Materials," Report No. SAND2019-11820 (2019).
- <sup>52</sup> E. N. Hahn, S. J. Fensin, T. C. Germann, and G. T. Gray, Acta Materialia **159**, 241 (2018).

This page left blank

# **DISTRIBUTION**

# Email—Internal

Name	Org.	Sandia Email Address
Shawn Pautz	01341	sdpautz@sandia.gov
Nathan Moore	01344	nwmoore@sandia.gov
James Carleton	01443	jbcarle@sandia.gov
Chad McCoy	01646	camccoy@sandia.gov
Andrew Vackel	01834	avackel@sandia.gov
Mike Leap	01834	mjleap@sandia.gov
Steven Hau	08256	skhau@sandia.gov
Michael Kracum	1834	mrkracu@sandia.gov
Jacob Mahaffey	1834	jtmahaf@sandia.gov
Shannon Murray	1834	semurr@sandia.gov
Technical Library	01977	sanddocs@sandia.gov

This page left blank



Sandia National Laboratories is a multimission laboratory managed and operated by National Technology & Engineering Solutions of Sandia LLC, a wholly owned subsidiary of Honeywell International Inc. for the U.S. Department of Energy's National Nuclear Security Administration under contract DE-NA0003525.